Supporting Information

Atomic Layer Deposited Interlayers for Robust Metal–Polymer Interfaces

Johanna Byloff,[†,‡] Claus O. W. Trost,[¶] Vivek Devulapalli,[†] Shuhel Altaf Husain,[§,‖] Damien Faurie,[§] Pierre–Olivier Renault,[‖] Thomas Edward James Edwards,[†,⊥] Megan J. Cordill,[¶] Daniele Casari,[†] and Barbara Putz[*,†,#]

†*Empa, Swiss Federal Laboratories for Materials Science and Technology, Laboratory for Mechanics of Materials and Nanostructures, Feuerwerkerstrasse 39, Thun, 3603, Switzerland*

‡*Laboratory for Nanometallurgy, ETH Zurich, Vladimir–Prelog–Weg 5, Zurich, 8093, Switzerland*

¶*Erich Schmid Institute of Materials Science, Austrian Academy of Sciences, Jahnstraße 12, Leoben, 8700, Austria*

§*LSPM–CNRS, UPR3407, Université Sorbonne Paris Nord, 99 Avenue Jean–Baptiste Clément 93430, Villetaneuse, France*

‖*Institut Pprime, CNRS – Université de Poitiers, 86073 Poitiers Cedex, France*

⊥*Research Center for Structural Materials, National Institute for Materials Science, 1-2-1 Sengen, Tsukuba 305-0047, Japan*

#*Department of Materials Science, Montanuniversität Leoben, Franz Josef Straße 18, Leoben, A–8700, Austria*

E-mail: barbara.putz@empa.ch

1 PVD Parameters

PVD deposition parameters for the Al top layer are summarized in Table S1 below.

Table S1: PVD parameters for deposition of the Al top layer

Interface type	native		artificial	
Testing method	uniaxial	biaxial	uniaxial	biaxial
Current [mA]	280	280	280	280
Ar flow rate [sscm]	10	10	10	10
Base pressure [mbar]	1.5×10^{-7}	1.9×10^{-5}	2.5×10^{-6}	8.7×10^{-8}
Working pressure [mbar]	9.8×10^{-3}	9.2×10^{-3}	7×10^{-3}	7×10^{-3}
Deposition rate [nm / s]	0.080	0.075	0.080	0.081

2 Additional IPF maps

Figure S1 shows ACOM IPF y maps of the investigated microstructures to ascertain the absence of thin film texture.

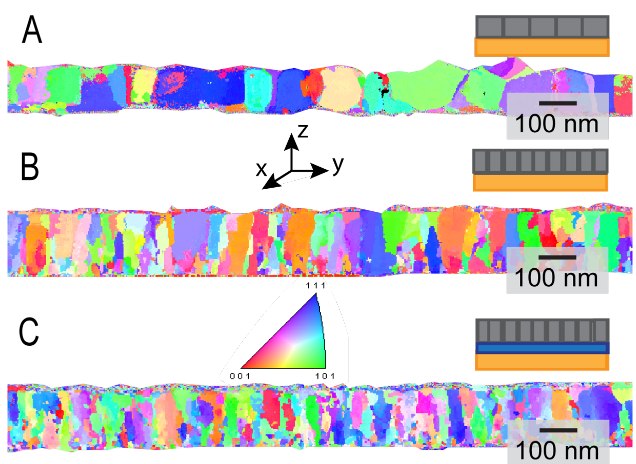

Figure S1: ACOM IPF y (in-plane direction) maps of the investigated Al microstructures. A, B: Al films on polyimide (native interlayer system). C: Al film with am–AlO_xH_y artificial ALD interlayer on polyimide. Grain boundaries are marked with black lines. Note that only the Al layer is shown.

3 FWHM evolution at different chi angles

For uniaxial XRD measurements, FWHM values at $\chi = 90°$ are shown in Figure S2 below. Regarding FWHM recovery during unloading, the data (parallel measurement, top and transverse, bottom) show a similar trend for native (A) and artificial (B) interface systems as biaxial FWHM measurements discussed in the main manuscript, however, as the signal intensity is lower for this experiment, the scatter is increased.

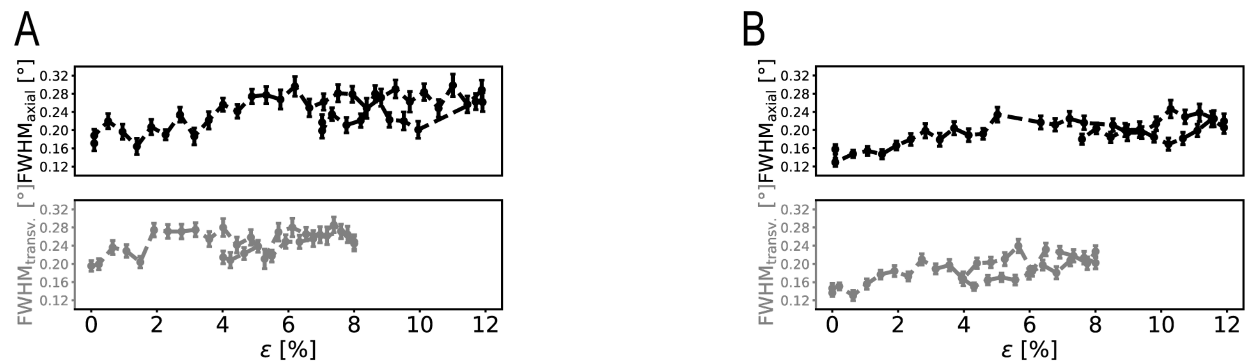

Figure S2: FWHM evolution as a function of applied strain at $\chi = 90°$ recorded during uniaxial measurements parallel (top) and transverse (bottom) to the tensile direction. A: native interlayer, B: artificial interlayer.

For the discussion of deformation domains for biaxial measurements, FWHM at $\chi = 90°$ (equivalent to $\psi = 0°$) is plotted in the manuscript (Figure 4) together with the Al film stress as a function of applied strain. Figure S3 shows all FWHM versus applied strain curves recorded at different χ angles during $\sin^2\psi$ analysis for Al/PI and am-AlO_xH_y interface systems, respectively, showing the same trends as the curves discussed in the main text.

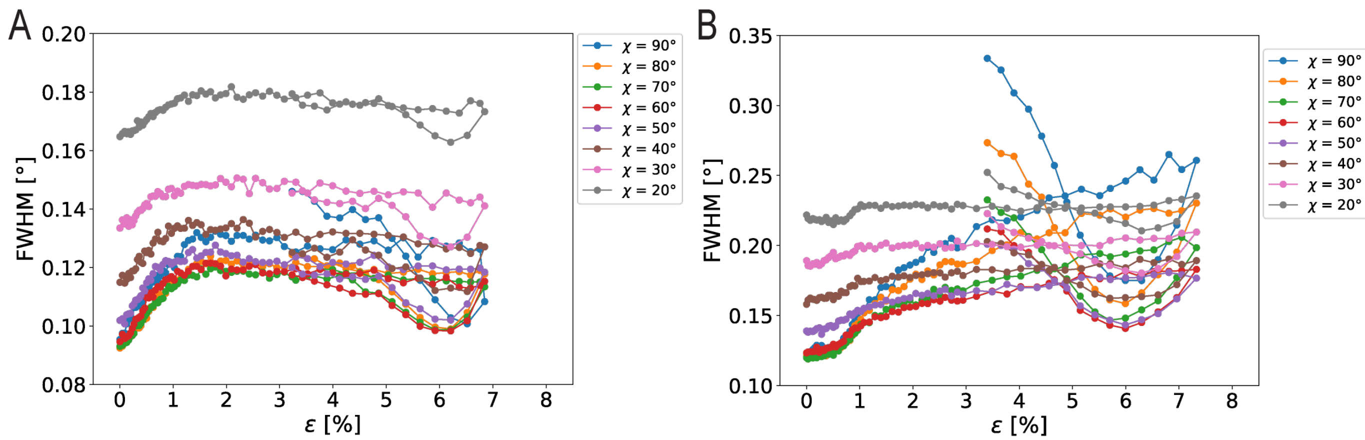

Figure S3: FWHM evolution as a function of applied strain recorded at different χ angles during $\sin^2\psi$ analysis for biaxial tensile straining. A: native interlayer, B: artificial interlayer. Note the different FWHM scales in A and B.

4 Post-mortem SEM images

Post-mortem SEM images of biaxially tested samples with mud-crack crack patterns are shown in Figure S4 below. Cracks visible on the surface are indicated with white arrows, growth hillocks with white circles.

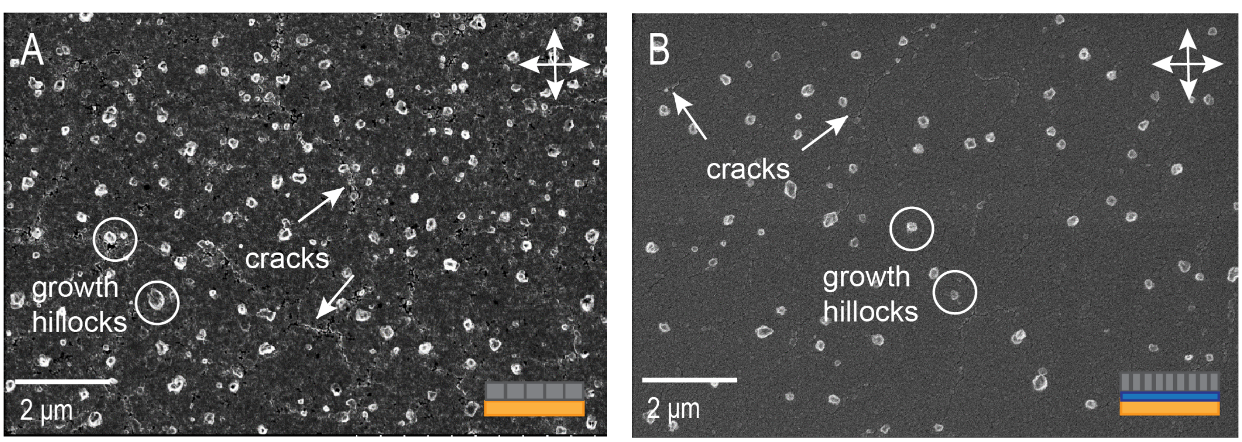

Figure S4: Post-mortem SEM images of equi-biaxially tested samples. A: Native interlayer system, B: artificial interlayer system. Hillocks grown during the deposition are indicated with white circles, while cracks are indicated with white arrows.

5 Theoretical yield stress calculations

The Hall–Petch (H-P) relation:[1]

$$\sigma_{yield,H-P} = \sigma_0 + K * d^{-\frac{1}{2}} \tag{S1}$$

with $\sigma_0 = 11.3$ MPa the bulk strength and $K = 0.07$ MPa $m^{\frac{1}{2}}$ the Hall–Petch constant[2] and the Nix model combined with the H-P relation:[3]

$$\sigma_{yield,Nix+H-P} = 3.464 * \frac{b}{2\pi * (1-\nu) * h} * \left[\frac{\mu_f * \mu_s}{\mu_f + \mu_s} * \ln(\frac{\beta_s * h}{b}) + \frac{\mu_f * \mu_o}{\mu_f + \mu_o} * \ln(\frac{\beta_o * t}{b}) \right] + \sigma_{yield,H-P} \tag{S2}$$

were used for yield stress calculations in the main manuscript, with $b = 0.286 * 10^{-9}$ (Burgers vector), $\beta_o = 17.4$, $\beta_s = 2.6$ (constants), $\mu_f = 24.8\ GPa$, $\mu_o = 178.9\ GPa$, $\mu_s = 1\ GPa$ (shear moduli of film, oxide, and substrate), $\nu = 0.31$ (Poisson's number), h (film thickness) and t (oxide thickness).

6 Additional resistance curves

To determine the adhesion energy and saturation crack and deformation spacings, as well as R/R_0 at high strains, samples were uniaxially loaded to 40% strain, with in-situ resistance measurements, the representative results of which are shown in Figure S5. COS and EFS values as well as the maximum $R/R_{0,max}$ ratio follow the same trend as the measurements presented in the manuscript, with an added artificial interlayer increasing both COS and EFS and decreasing $R/R_{0,max}$.

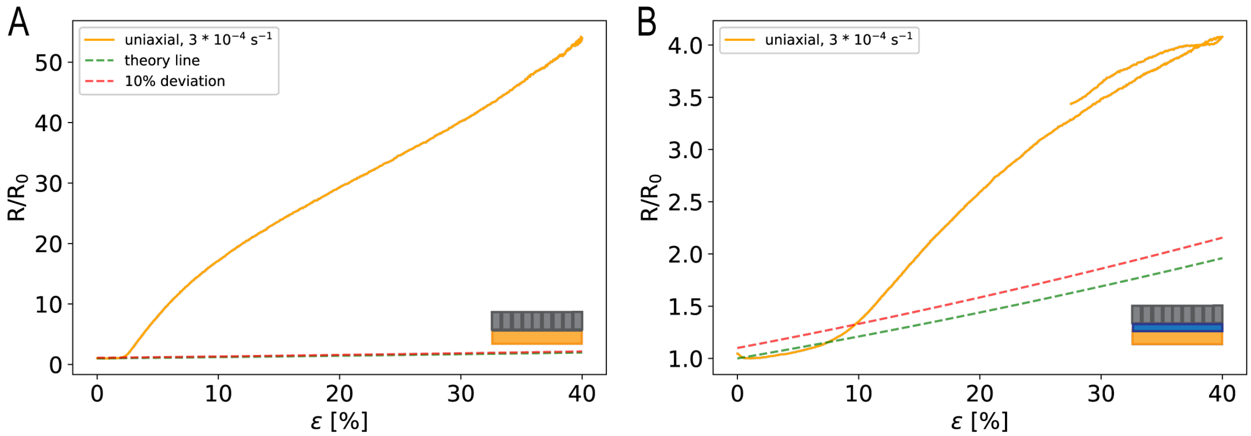

Figure S5: In-situ resistance curves of native (A) and artificial (B) interlayer samples tested to 40% uniaxial strain. Note the different R/R_0 scales.

7 Adhesion energy calculation

Buckle geometry measurements for both native and artificial interlayer systems (δ = height and b = half width of the buckle) are reported in Figure S6.

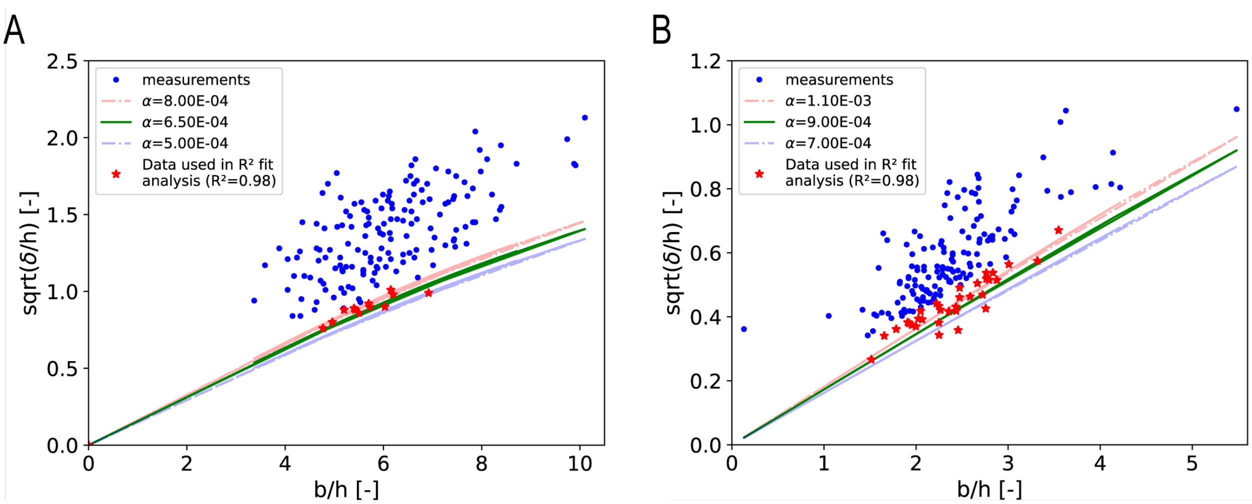

Figure S6: Adhesion analysis of native (A) and artificial (B) interlayer systems using the TID model. Upper and lower bounds for the fitted α value (green line) are marked with red and blue dashed lines, respectively. The data used for the R^2 analysis of the fitting function is marked with star symbols.

Measured values can be fitted with the α value using the tensile induced delamination *(TID)* model,[4]

$$\sqrt{\frac{\delta}{h}} = (2\alpha)^{\frac{1}{4}} \frac{b}{h} \left(1 + \sqrt{1 + \frac{3}{4}\alpha \frac{b}{h}^4}\right)^{-\frac{1}{4}} \tag{S3}$$

where α is directly related to the adhesion energy Γ via:

$$\alpha = \frac{4\Gamma}{hE'_f}(\frac{2}{\pi})^4 \tag{S4}$$

with $E'_f = E_f/(1-\nu_f^2)$ ($E'_f = 7.95 \times 10^{10}$) as the modified Young's modulus to account for the Poisson effect. Average α values of 6.5×10^{-4} (native) and 9.0×10^{-4} (artificial) were used in the analysis to provide a lower bound for the adhesion energy. Average α values were chosen to be within 10% deviation of the lowest data points. Upper and lower bounds for this value are shown in Figure S4. An R^2 fit analysis was applied to a subset of the data (red stars) to determine the fit correspondence.

References

(1) Hall, E. O. The Deformation and Ageing of Mild Steel: III Discussion of Results. *Proceedings of the Physical Society. Section B* **1951**, *64*, 747.

(2) Cordero, Z. C.; Knight, B. E.; Schuh, C. A. Six decades of the Hall–Petch effect – a survey of grain-size strengthening studies on pure metals. *International Materials Reviews* **2016**, *61*, 495 – 512.

(3) Nix, W. D. Mechanical properties of thin films. *Metallurgical Transactions A* **1989**, *20*, 2217–2245.

(4) Cordill, M.; Fischer, F.; Rammerstorfer, F.; Dehm, G. Adhesion energies of Cr thin films on polyimide determined from buckling: Experiment and model. *Acta Materialia* **2010**, *58*, 5520–5531.